Electronic Supplementary Material (ESI) for Soft Matter.

Supplementary Materials for:

Angle-resolved optical spectroscopy of photonic cellulose nanocrystal films reveals the influence of additives on the mechanism of kinetic arrest.

Thomas G. Parton, Richard M. Parker, Sonja Osbild, Silvia Vignolini* and Bruno Frka-Petesic*

* silvia.vignolini@mpikg.mpg.de

* bf284@cam.ac.uk

Contents

S01 Discussion of different concentration metrics

This section provides an overview of different expressions for the concentration of species in a colloidal dispersion. Consider a system containing CNC, water, an additive in the CNC dispersion (da) and an additive that is not in the CNC dispersion (na). Depending on the circumstances, it is convenient to either consider the concentration of each species relative to the total system (including all four components), the colloidal dispersion (excluding the undissolved additive) or solution (only the water and dissolved additive). These three cases are illustrated in **Fig. S1**, and the system volume is each case is

$$V_{\text{tot}} = V_{\text{CNC}} + V_{\text{wat}} + V_{\text{da}} + V_{\text{na}} \quad (1)$$

$$V_{\text{dis}} = V_{\text{CNC}} + V_{\text{wat}} + V_{\text{da}} \quad (2)$$

$$V_{\text{sol}} = V_{\text{wat}} + V_{\text{da}} \quad (3)$$

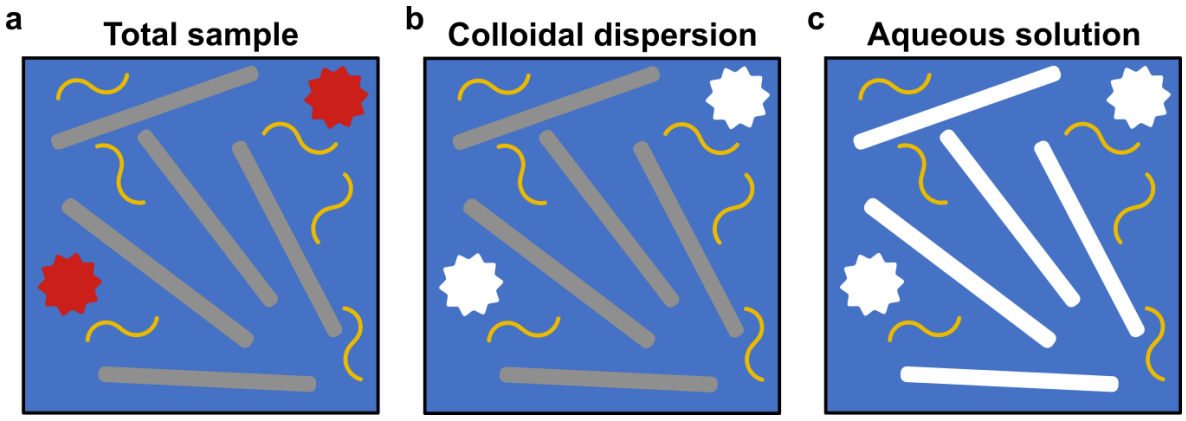

Fig. S1 Illustration (not to scale) representing the different components of the sample: the CNCs (grey rods), dissolved additive (orange lines), undissolved additive (red stars) and water (blue). Within the total sample (a), the colloidal dispersion (b) comprises all components in the aqueous phase (CNCs, dissolved additive and water, as shown in colour in b). In contrast, the aqueous solution (c) comprises only the water and dissolved additive.

First, the concentration can be expressed as a proportion of the total sample mass or volume, in terms of volume fraction

$$\Phi_{\text{i}} = V_i / V_{\text{tot}} \quad (4)$$

or mass fraction

$$w_i = \frac{m_i}{m_{\text{tot}}} = \frac{\rho_i V_i}{\sum_j \rho_j V_j} \quad (5)$$

In general, the volume fraction can be calculated from the mass fraction (and vice versa) if the composition of the sample and the density of each component is known. In particular, for a binary mixture of materials a and b (where $\Phi_a + \Phi_b = 1$ and $w_a + w_b = 1$) the volume and mass fractions are related by

$$w_a = \frac{\rho_a \Phi_a}{\rho_a \Phi_a + \rho_b (1 - \Phi_a)} \quad (6)$$

$$\Phi_a = \frac{\rho_a^{-1} w_a}{\rho_a^{-1} w_a + \rho_b^{-1} (1 - w_b)} \quad (7)$$

Eq. 7 is used to estimate the CNC volume fraction of the initial stock suspensions by thermogravimetric analysis (see Experimental Methods of the main text).

If the sample contains non-dispersed additive ($V_{na} \neq 0$), the effective concentrations within the dispersion can be defined. In the main text, the effective volume fraction of species i is used, which is given by

$$\widetilde{\Phi}_i = V_i / V_{\text{dis}}. \quad (8)$$

Finally, if the additive is an ionic species i, it is useful to consider its molar concentration c_i (mol/L) or mass concentration γ_{i} (g/L) in the aqueous solution. The molar concentration of a given species i in a solution is given by

$$c_{\text{i}} = \frac{N_i}{V_{\text{sol}}}, \quad (9)$$

where N_i is the number of moles of i. Similarly, the mass concentration of i is

$$\gamma_{\text{i}} = \frac{m_i}{V_{\text{sol}}}, \quad (10)$$

where m_i is the total mass of i in the solution. The two concentrations are related by $\gamma_{\text{i}} = M_{\text{i}} c_{\text{i}}$ where M_{i} is the molar mass of i.

As the concentrations of the initial CNC suspension and electrolyte solutions used for mixing are determined gravimetrically (i.e., by mass), the ion:CNC ratio can be directly calculated from experimental data as a mass ratio

$$\mu_i = \frac{m_i}{m_{\mathrm{CNC}}} \quad (11)$$

which can then be used to estimate the ion:CNC volume ratio

$$\nu_i = \frac{V_i}{V_{\mathrm{CNC}}} = \mu_i \frac{\rho_{\mathrm{CNC}}}{\rho_i} \quad (12)$$

where ρ_{CNC} and ρ_{i} are the mass densities of CNC and ion salt, respectively. However, to compare different ionic species, it is most convenient to express this ratio in terms of moles of added ions per CNC dry mass,

$$\hat{c}_i = \frac{N_i}{m_{\mathrm{CNC}}} = \frac{\mu_i}{M_i}, \quad (13)$$

where M_i is the molar mass.

The absolute concentration of added ions in aqueous solution at a given CNC concentration, c_i, is given by

$$c_i = \frac{N_i}{V_{\mathrm{sol}}} = \frac{\hat{c}_i \, \rho_{\mathrm{CNC}}}{\nu_{\mathrm{wat}} + \nu_i}. \quad (14)$$

where V_{sol} is the volume of the solution (i.e., excluding the volume occupied by the CNCs), and ν_{wat} is the water:CNC volume ratio. As the volume of ions is negligible, $\nu_i \approx 0$, $\Phi_{\mathrm{CNC}} = (1 + \nu_{\mathrm{wat}})^{-1}$, and the molar concentration of ions in solution is given by

$$c_i = \frac{\rho_{\mathrm{CNC}} \Phi_{\mathrm{CNC}}}{1 - \Phi_{\mathrm{CNC}}} \hat{c}_i. \quad (15)$$

S02 Pitch compression plot

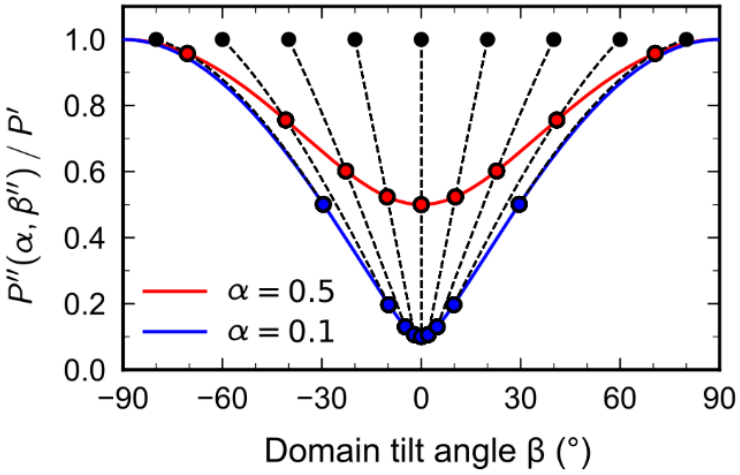

Fig. S2 Relative change in pitch with final domain tilt angle $P''(\alpha, \beta'') \,/\, P'$, given by Eqs. 2 and 3 of the main text. Curves are shown for $\alpha = 0.5$ (red) and $\alpha = 0.1$ (blue). Black dotted lines indicate the evolution in $P''(\alpha, \beta'') \,/\, P'$ with decreasing α for fixed initial tilt angle β'.

S03 TEM size distributions

For transmission electron microscopy (TEM), a dilute CNC suspension (approx. 0.001 wt%) was prepared in an aqueous solution of sulfuric acid (10 mM), and carbon-coated copper TEM grids (AGS160-3, Agar Scientific) were glow-discharged (Quorum GloQube, 25 mA current, <0.1 mbar vacuum). A 4 µL droplet of the CNC suspension was then deposited onto the grid for 120 seconds, before blotting away the excess liquid using filter paper. A 4 µL droplet of 2 wt% uranyl acetate solution was then deposited onto the grid for 90 seconds before blotting. The grid was then left to dry in air. TEM was performed using a Talos F200X G2 microscope (Thermo Scientific FEI Company) at 200 kV and images were acquired using a CMOS camera (Ceta 4k x 4k). An example image is shown in **Fig. S3a**.

The morphological properties of the CNCs were obtained as previously described.[1] Briefly, the outlines of 160 negatively-stained CNCs were manually traced in ImageJ to produce a binary image (**Fig. S3b**), from which the basic morphological properties were extracted automatically using the Shape Filter plugin.[2] Any isolated object in the TEM was assumed to be a single CNC particle, including those that could be interpreted as two overlapping rod-like particles.

The irregular shape of CNCs permits many possible definitions of their length, width etc. From oriented bounding boxes drawn around the particles (exemplified in **Fig. S3b**), histograms were obtained for the box length L_b (**Fig. S3c**), box width W_b (**Fig. S3d**) and corresponding aspect ratio $a_b = L_b/W_b$ (**Fig. S3e**). Using the true particle area A, (**Fig. S3f**), the area-equivalent width $W_{AE} = A/L_b$ (**Fig. S3g**) and corresponding aspect ratio $a_{AE} = L_b/W_{AE}$ (**Fig. S3h**) can also be defined. CNCs exhibit considerable polydispersity in size, typically following a log-normal distribution. For each morphological property Z, **Table S1** shows the mean and standard deviation, as well as the log mean and log standard deviation (i.e. mean and standard deviation for $ln\, Z$ in the units shown in the first column).

Property	Mean	Standard deviation	Log mean	Log standard deviation
Box length (nm)	139	102	4.72	0.64
Box width (nm)	26	21	3.01	0.70
Box aspect ratio	6.07	2.72	1.71	0.42
Area (nm^2)	2410	2980	7.21	1.09
Area-equivalent width (nm)	13.7	7.2	2.49	0.52
Area-equivalent aspect ratio	10.2	4.9	2.23	0.43

119 **Table S1** Statistics for morphological properties obtained from 160 CNC outlines in TEM images.

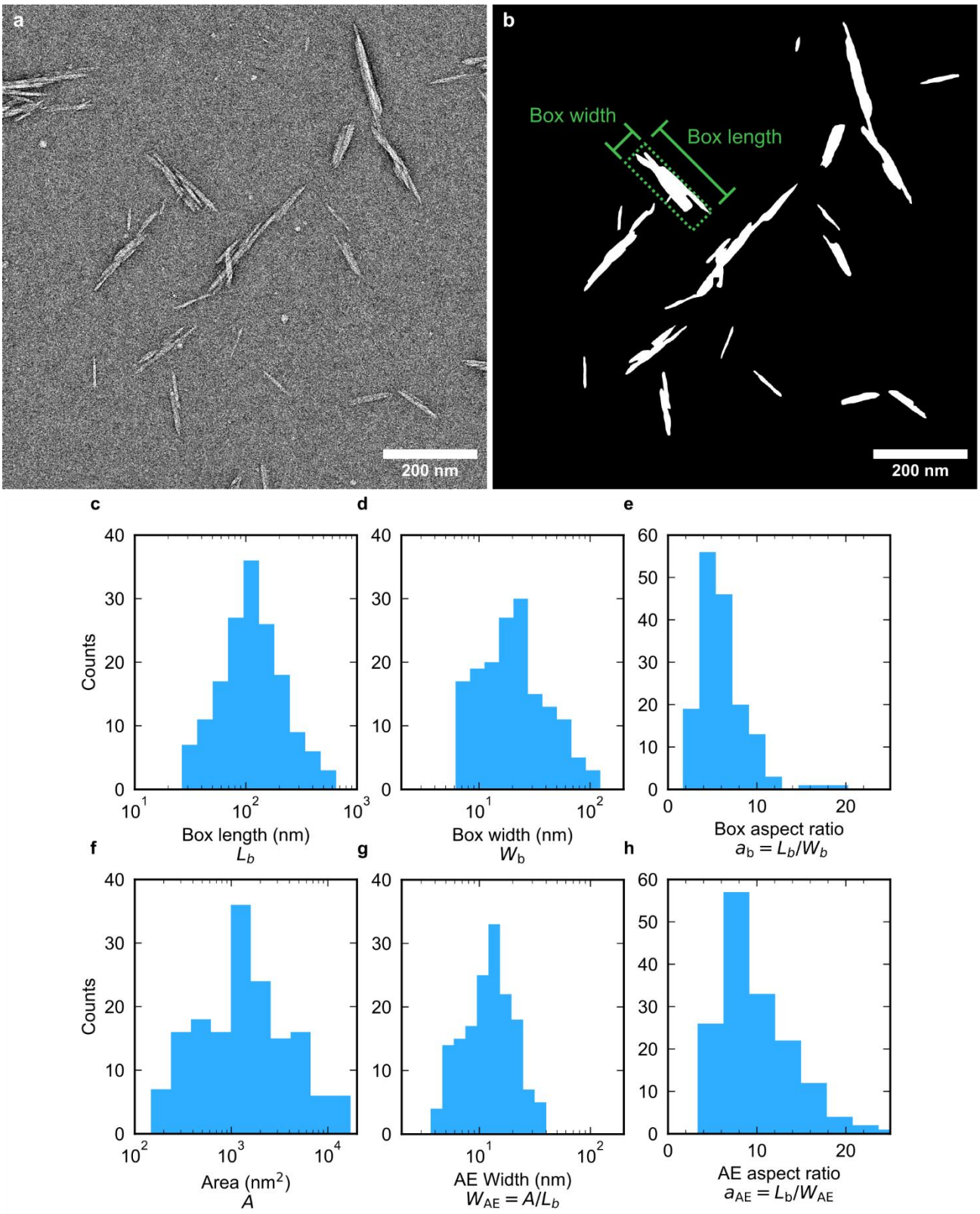

Fig. S3 (a) Example TEM image of negatively-stained CNCs. (b) Binary image obtained from (a) by manual tracing of particle outlines. Green annotations show the definition of the oriented bounding box for an example outline. (c-h) Histograms for the key morphological properties listed in **Table S1**.

S04 Micro-spectroscopy for photonic films prepared with H-CNCs and added NaCl

Micro-spectroscopy was performed alongside the polarised optical microscopy described in the main text. One end of an optical fibre (Avantes FC-UV600-2-SR, core diameter 600 µm) was positioned in the confocal image plane of the microscope, while the other end was coupled to a UV-vis spectrometer (Avantes AvaSpec-HS2048). LCP and RCP reflectance spectra were normalised to the reflection from a silver mirror (Thorlabs PF10-03-P01) imaged under the corresponding polarisation conditions.

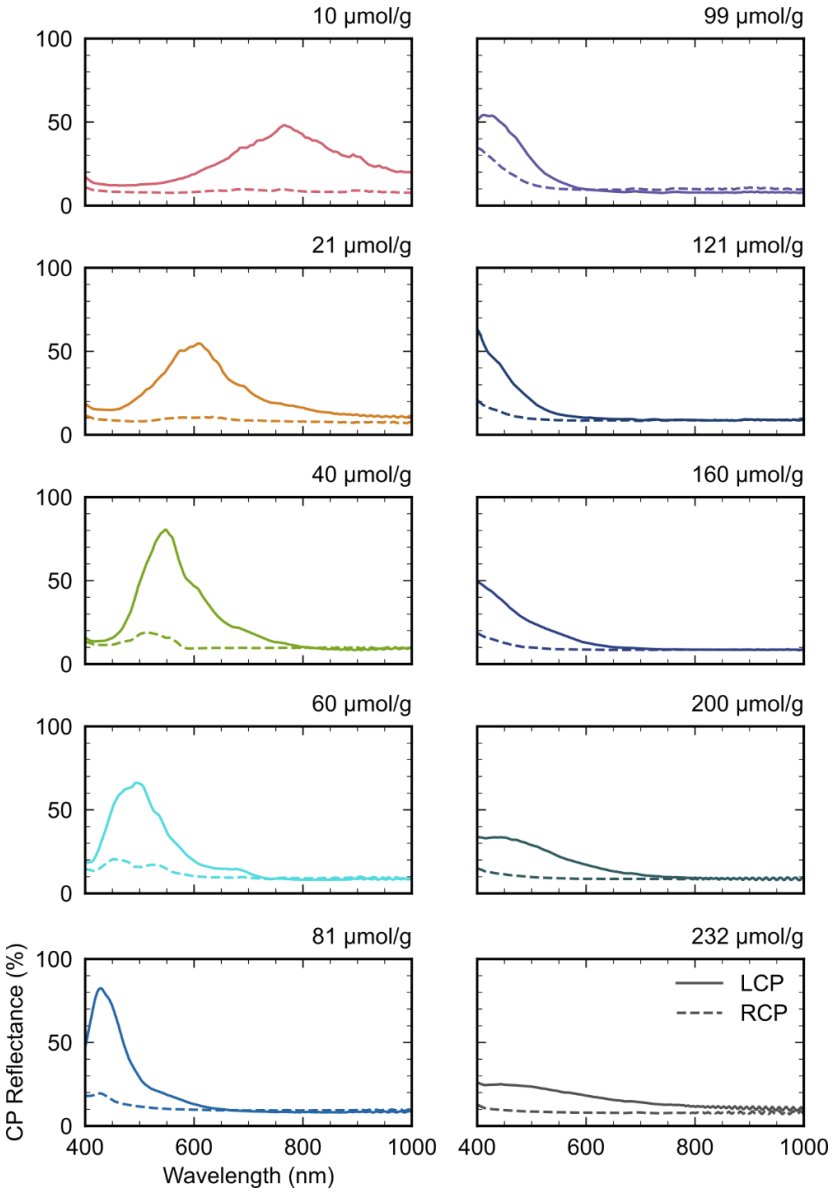

Fig. S4 Reflectance micro-spectra for selected photonic films prepared using H-CNCs and added NaCl ($\hat{c}_{NaCl}$ = 0 – 232 µmol/g). Solid and dashed lines correspond to LCP and RCP spectra, respectively. Spectra were acquired from the regions shown in the POM images in **Fig. 3** of the main text.

S05 SEM cross-sections for photonic films prepared with H-CNCs and NaCl

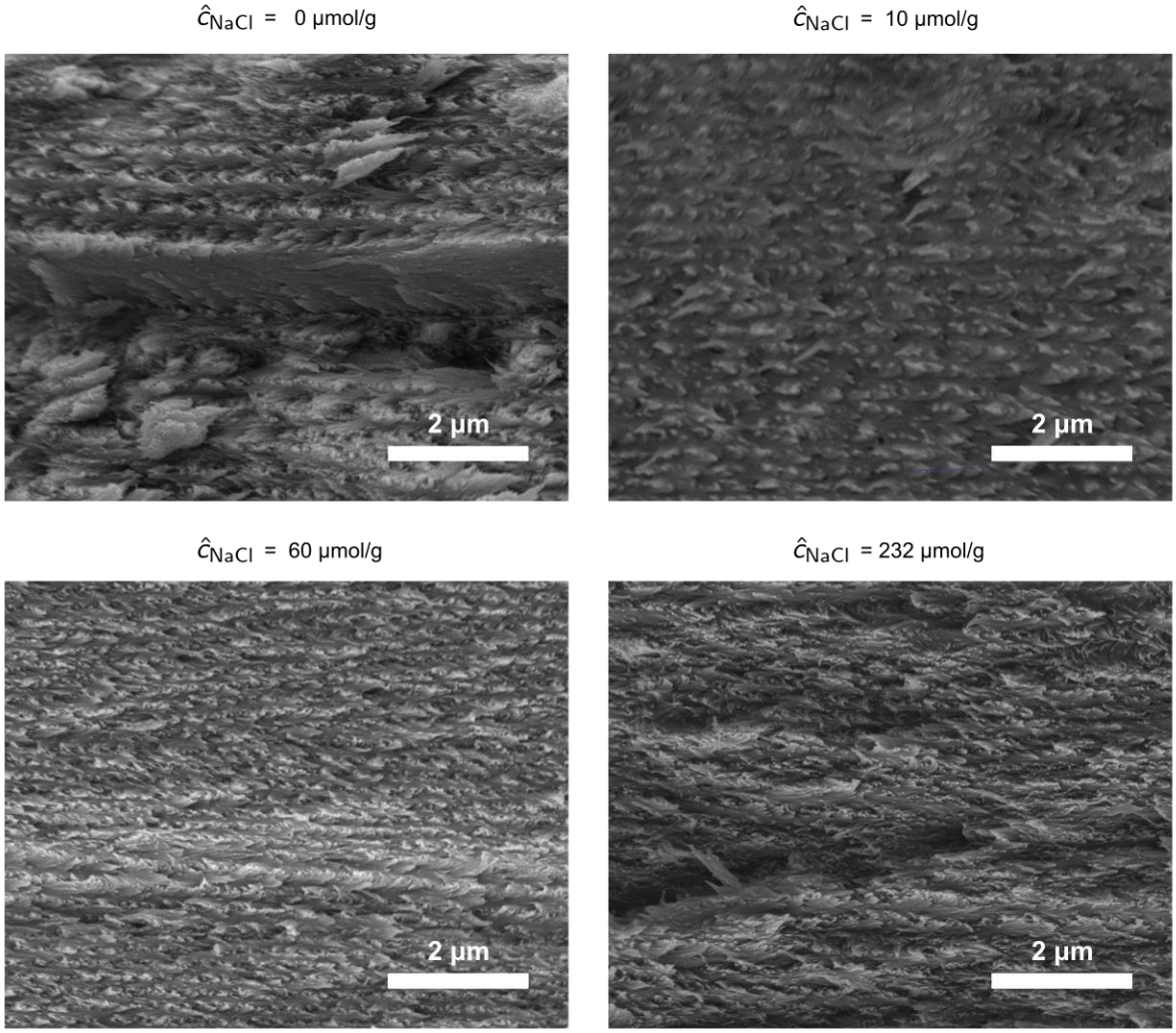

Fig. S5 Cross-sectional SEM images for selected photonic films prepared using H-CNCs and NaCl ($\hat{c}_{NaCl}$ = 0, 10, 40, 60 and 232 μmol/g). The image orientation matches the film, such that the surface normal lies in the vertical direction for each image. The $\hat{c}_{NaCl}$ = 0 μmol/g sample has an apparent pitch corresponding to IR reflection, while for other samples the pitch is generally consistent with the POM and AROS data. Note that pitch increases sharply for tilted domains (most notable in the image for the 60 μmol/g sample).

S06 Origins of the features in the AROS data

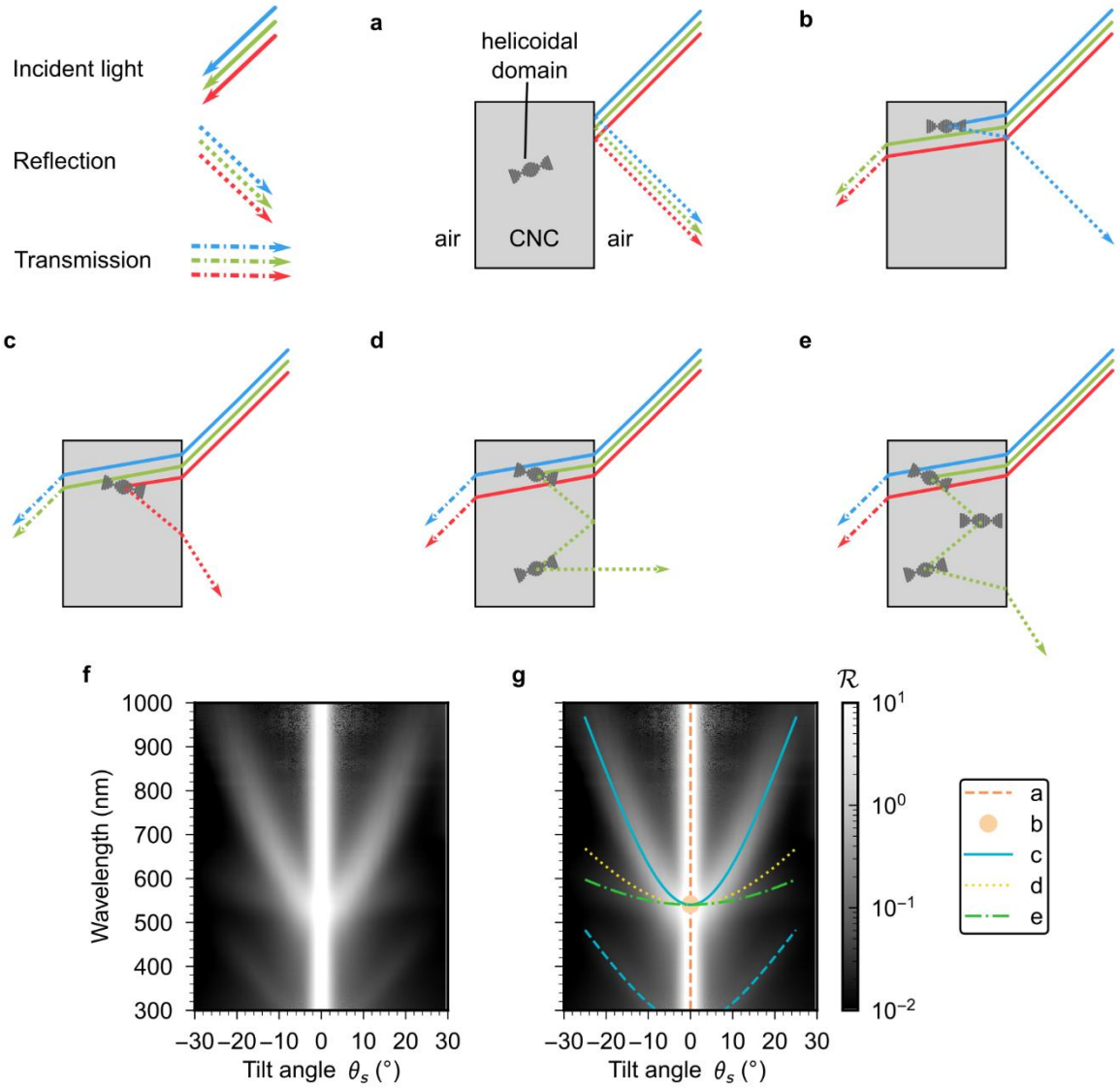

Fig. S6 (a-e) Illustrations of possible spectral features in AROS data. (a) Broadband reflection from the air-CNC interface due to refractive index contrast (unrelated to any helicoidal ordering). (b) Selective reflection by an aligned helicoidal domain. (c) Selective reflection by a tilted helicoidal domain. (d) Reflection from two helicoidal domains via the CNC-air interface. (f) Reflection from three helicoidal domains. (f) AROS data (log-scale reflectance) for a photonic CNC film with λ_0 = 536 nm, exhibiting several spectral features. (g) Data from (f) with lines overlaid corresponding to illustrations (a-e). The blue dashed curve corresponds to the second-order (λ/2) reflection from tilted domains (not represented in d).

S07 Conductometric titration

Conductometric titration was performed using an automatic titrator (Metrohm 856). The titrand (47.7 mg CNC dry mass) was prepared by diluting 2.013 g of stock CNC suspension (2.43 wt%) into 200 mL of 0.5 mM NaCl solution. The titration was performed by injecting NaOH solution (10.0 mM) in 5 µL increments using a burette, while continuously recording the suspension conductivity. The number of sulfate half-esters per CNC dry mass (in µmol/g) was determined from the first equivalence point of the titration curve using a manual piecewise linear fitting (**Fig. S7**).

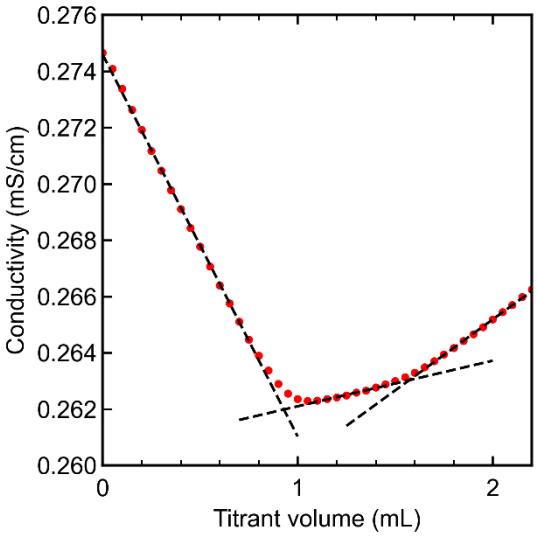

Fig. S7 Conductometric titration of H-CNC suspension against base solution. The first equivalence point at 0.93 mL corresponds to a CNC surface charge of 196 µmol/g.

S08 POM and AROS for photonic films prepared with Na-CNCs and added NaCl

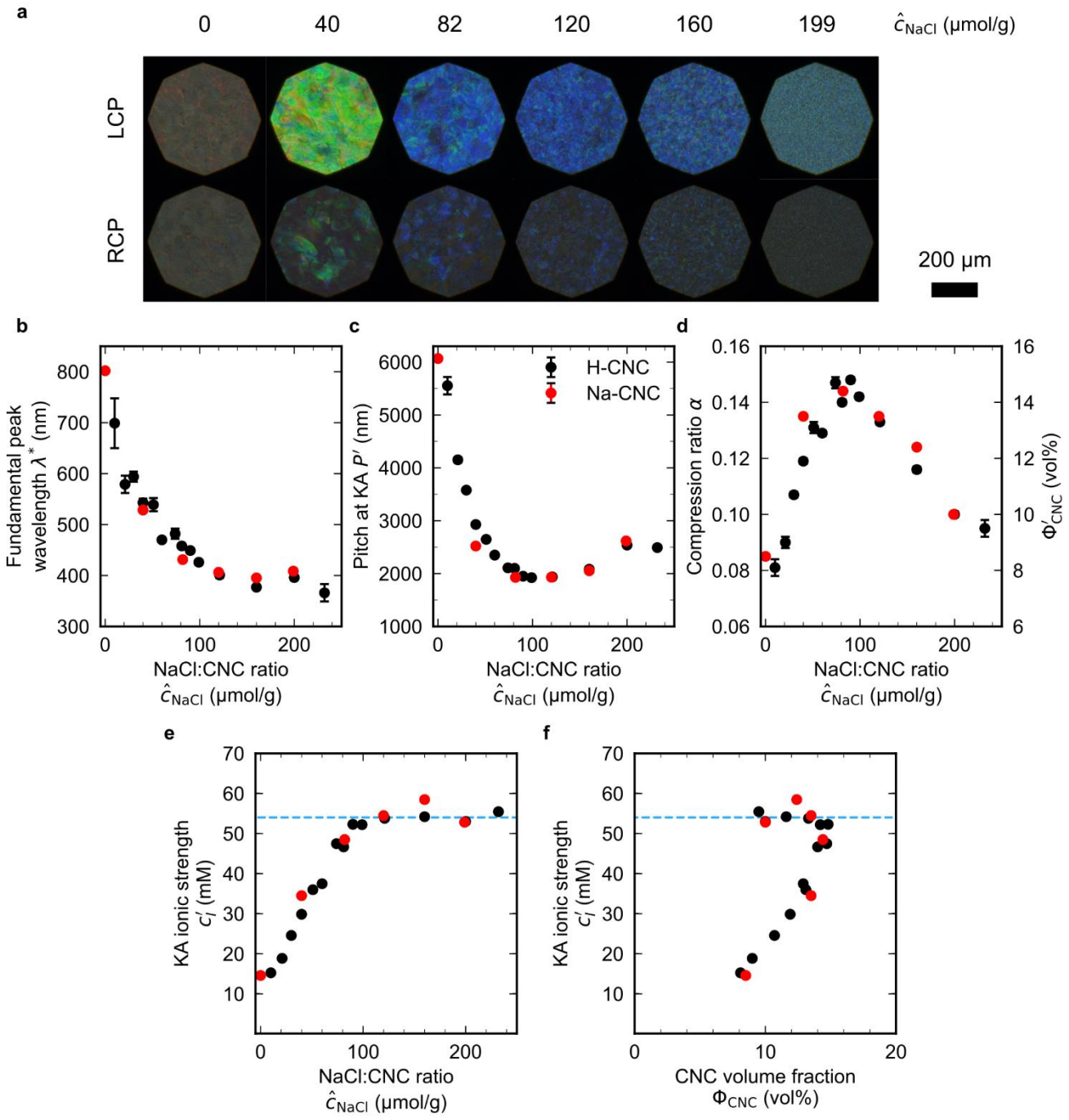

Fig. S8 POM and AROS for photonic films prepared with Na-CNCs and NaCl. The original H-CNC suspension (2.37 wt%) was neutralised using 10 mM NaOH solution. Due to the lower concentration of the resulting Na-CNC suspension (1.26 wt%), films were cast using 6.0 mL of 1.0 wt% suspension (rather than 3.0 mL of 2.0 wt% suspension, as used for all other films). (a) POM images of photonic CNC films with $\hat{c}_{NaCl}$ for Na-neutralised suspension (Na-CNC). (b-d) AROS fitting parameters for the Na-CNC films (red), which show very similar trends to the H-CNC series from the main text (black). (e) Ionic strength at KA, c'_I, versus $\hat{c}_{NaCl}$. (f) c'_I versus Φ'_{CNC}. Blue dashed lines correspond to c'_I = 54 mM, as in the main text.

S09 POM and AROS for photonic films prepared with H-CNCs and added $CaCl_2$

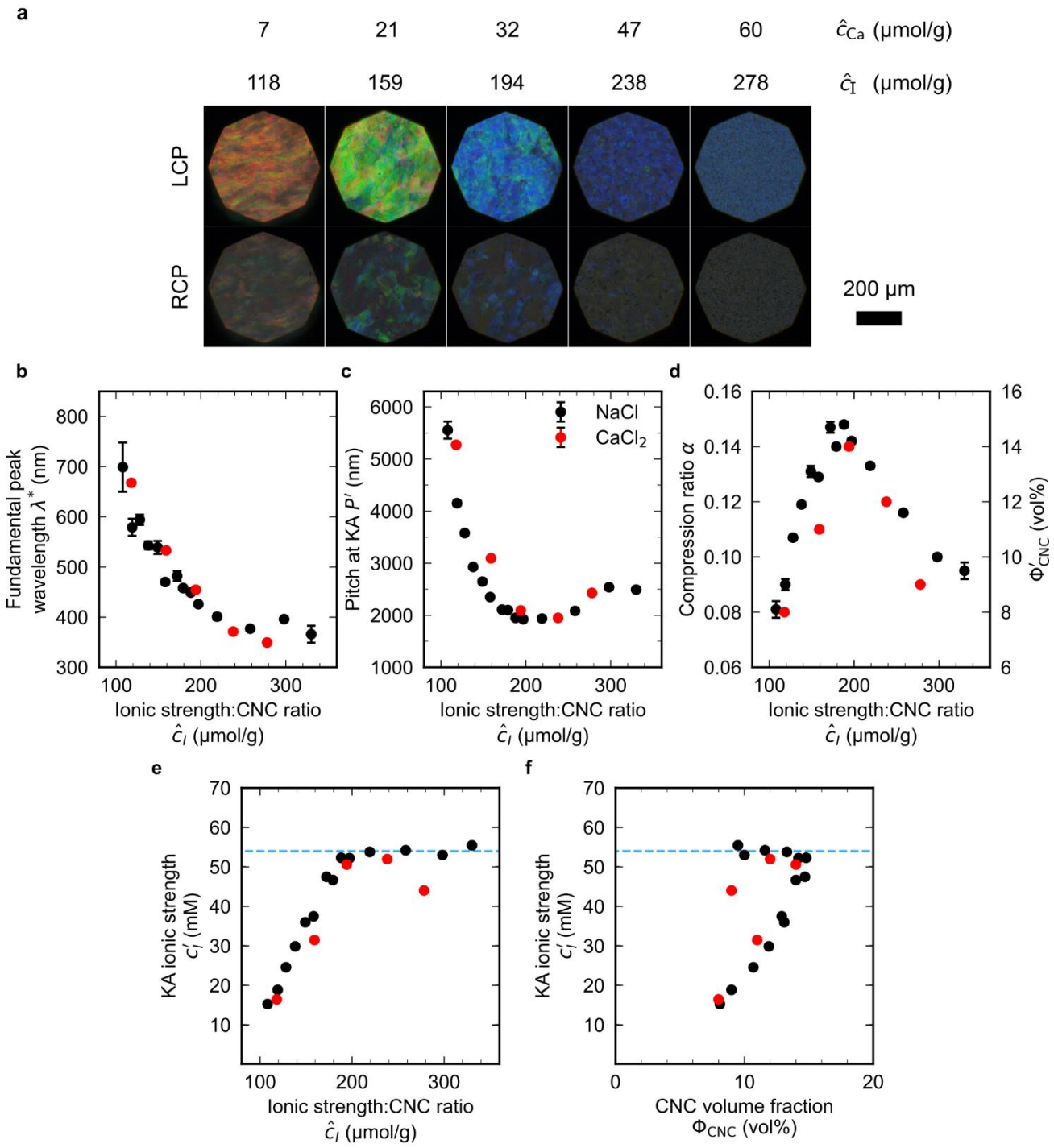

Fig. S9 (a) POM images of photonic CNC films with increasing $CaCl_2$:CNC ratio (expressed as $\hat{c}_{Ca}$, and as ionic strength per CNC mass $\hat{c}_I$). (b-d) AROS fitting parameters λ^*, P', α for H-CNC films with $CaCl_2$ (red). The H-CNC NaCl series from the main text (black) is also shown for comparison. (e) Ionic strength at KA, c'_I, versus $\hat{c}_I$ (f) c'_I versus Φ'_{CNC}. Blue dashed lines correspond to c'_I = 54 mM, as in the main text.

S10 Rationalising the concurrent effects of added ions on CNC self-assembly

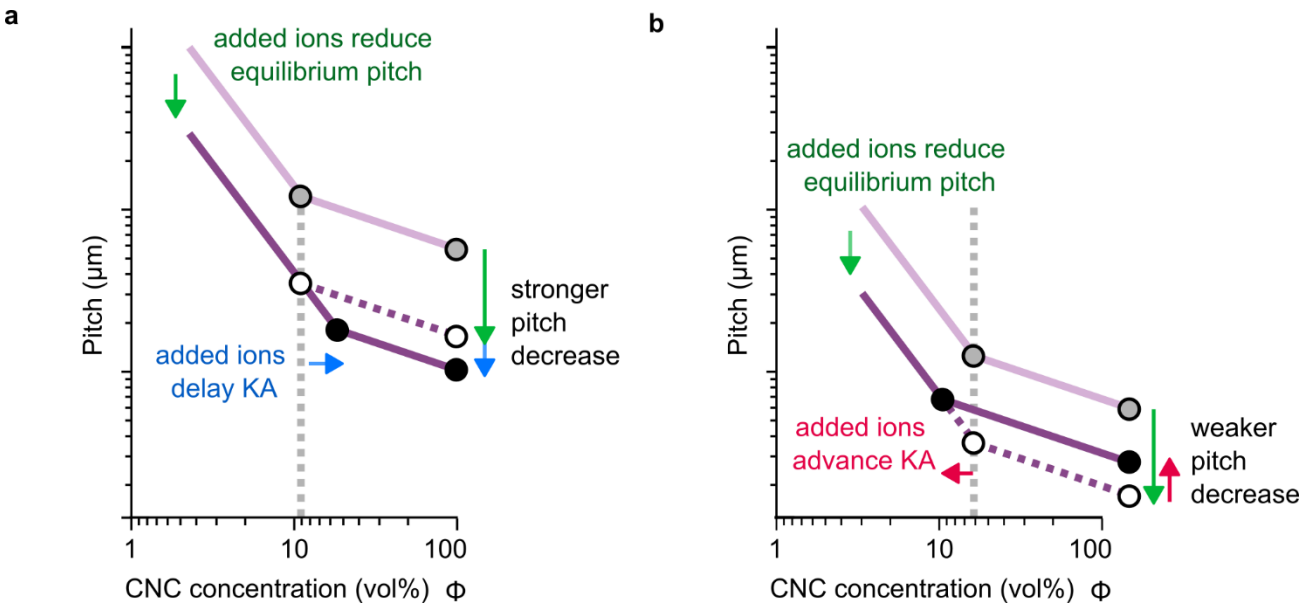

Fig. S10 Rationalising the variation in λ^* with $\hat{c}_{\mathrm{NaCl}}$ by considering the concurrent effects of increasing ion-CNC ratio $\hat{c}_{\mathrm{NaCl}}$ on the pitch evolution for (a) low and (b) high $\hat{c}_{\mathrm{NaCl}}$ values. At low $\hat{c}_{\mathrm{NaCl}}$ values (a), increasing $\hat{c}_{\mathrm{NaCl}}$ is expected to both reduce the equilibrium pitch at all concentrations (green arrow) and to delay KA (blue arrow), which lead to a strong reduction in pitch. In contrast, at high $\hat{c}_{\mathrm{NaCl}}$ values (b), the earlier KA (red arrow) partially counter-acts the reduction in equilibrium pitch with increasing $\hat{c}_{\mathrm{NaCl}}$, leading to a weaker decrease in P'' with $\hat{c}_{\mathrm{NaCl}}$. This illustration assumes that in the pre-KA regime the pitch decreases with a power-law dependence $P(\Phi_{\mathrm{CNC}}) \sim \Phi_{\mathrm{CNC}}^{-\eta}$ with exponent $\eta > 1$, and in the post-KA regime the pitch decreases according to $P(\Phi_{\mathrm{CNC}}) \sim \Phi_{\mathrm{CNC}}^{-1}$.

S11 Modified compression model

Consider a sample that consists of CNCs, water, additives dispersed in the CNC suspension (da), and additives that are not part of the CNC dispersion (na). In this case, one can define an *effective* CNC volume fraction considering only the dispersion, given by

$$\widetilde{\Phi}_{\mathrm{CNC}} = \frac{V_{\mathrm{CNC}}}{V_{\mathrm{dis}}} = \frac{V_{\mathrm{CNC}}}{V_{\mathrm{CNC}} + V_{\mathrm{wat}} + V_{\mathrm{da}}} \quad (16)$$

The effective compression of the CNC dispersion upon drying is then given by

$$\tilde{\alpha} = \frac{V''_{\mathrm{dis}}}{V'_{\mathrm{dis}}} = \frac{\widetilde{\Phi}'_{\mathrm{CNC}}}{\widetilde{\Phi}''_{\mathrm{CNC}}} \quad (17)$$

and is less than the macroscopic compression of the overall film (Eq. 2 of the main text). In terms of volume ratios, the overall and effective CNC volume fractions are then respectively given by

$$\Phi_{\mathrm{CNC}} = (1 + \nu_{\mathrm{da}} + \nu_{\mathrm{na}} + \nu_{\mathrm{wat}})^{-1} \quad (18)$$

and

$$\widetilde{\Phi}_{\mathrm{CNC}} = (1 + \nu_{\mathrm{da}} + \nu_{\mathrm{wat}})^{-1}, \quad (19)$$

while the overall and effective compression ratios are respectively given by

$$\alpha = \frac{1 + \nu''_{\mathrm{da}} + \nu''_{\mathrm{na}} + \nu''_{\mathrm{wat}}}{1 + \nu'_{\mathrm{da}} + \nu'_{\mathrm{na}} + \nu'_{\mathrm{wat}}} \quad (20)$$

and

$$\tilde{\alpha} = \frac{1 + \nu''_{\mathrm{da}} + \nu''_{\mathrm{wat}}}{1 + \nu'_{\mathrm{da}} + \nu'_{\mathrm{wat}}}. \quad (21)$$

If the additive is fully dissolved at KA ($\nu_{\mathrm{na}} = 0$) then $\widetilde{\Phi}_j = \Phi_j$ and $\tilde{\alpha} = \alpha$, and the equations reduce to those for the reduced compression model (Eqs. 6 and 7 of the main text).

Fitting of AROS data is expected to yield the effective parameters $\tilde{\alpha}$, P' and $\lambda^* = nP'\tilde{\alpha}$. However, these quantities cannot be immediately related to the equations above, as only the total user-defined additive:CNC ratio $\nu_{\mathrm{add}} = \nu_{\mathrm{da}} + \nu_{\mathrm{na}}$ is known *a priori*. It is possible to lift this uncertainty by assuming that ν_{da} corresponds to the additive solubility, which is typically reported as $\gamma^{(s)}_{\mathrm{add}}$ (in mg/mL):

$$\gamma_{\text{add}}^{(s)} = \frac{m_{\text{da}}}{V'_{\text{sol}}} \quad (22)$$

which can be re-written in terms of volume ratios as

$$\frac{1}{\gamma_{\text{add}}^{(s)}} = \frac{V'_{\text{sol}}}{\rho_{\text{add}}\, V_{\text{da}}} = \frac{1}{\rho_{\text{add}}} \frac{\nu'_{\text{wat}} + \nu'_{\text{da}}}{\nu'_{\text{da}}}. \quad (23)$$

This equation can be re-arranged to obtain

$$\nu'_{\text{wat}} = \left(\frac{\rho_{\text{add}}}{\gamma_{\text{add}}^{(s)}} - 1 \right) \nu'_{\text{da}}. \quad (24)$$

To make further progress, it can be assumed that KA occurs at a critical effective CNC volume fraction (i.e. a similar assumption to that made in the reduced compression model, but using $\widetilde{\Phi}'_{\text{CNC}}$ rather than Φ'_{CNC}. If $\widetilde{\Phi}'_{\text{CNC}} = \tilde{\alpha}_0$, where $\tilde{\alpha}_0 = \alpha_0$ is the compression ratio for a no-additive film, then Eqs. 17 and 19 give

$$\tilde{\alpha} = \frac{\alpha_0}{\widetilde{\Phi}''_{\text{CNC}}} = \alpha_0 \, (1 + \nu_{\text{da}}) \quad (25)$$

where the superscript for $\nu'_{\text{da}} = \nu''_{\text{da}}$ has been dropped for convenience. From Eq. 24, it can then be shown that

$$\frac{1}{\tilde{\alpha}_0} = 1 + \nu_{\text{da}} + \nu'_{\text{wat}} = 1 + \left(\frac{\rho_{\text{add}}}{\gamma_{\text{add}}^{(s)}} \right) \nu_{\text{da}} \,. \quad (26)$$

The effective compression ratio at high additive loadings reaches a saturation value $\tilde{\alpha}_{\text{sat}}$ given by:

$$\tilde{\alpha}_{\text{sat}} = \alpha_0 \, (1 + \nu_{\text{sat}}) \,, \quad (27)$$

where

$$\nu_{\text{sat}} = \frac{(1 - \alpha_0)}{\alpha_0} \left(\frac{\gamma_{\text{add}}^{(s)}}{\rho_{\text{add}}} \right), \quad (28)$$

Eq. 28 is valid for samples where $\gamma_{\text{add}}^{(s)} < \gamma'_{\text{da}}$. If the additive is entirely dispersed prior to KA ($\gamma_{\text{add}}^{(s)} > \gamma'_{\text{da}}$) then $\tilde{\alpha} = \alpha$. In the limit of an entirely insoluble additive ($\gamma_{\text{add}}^{(s)} \to 0$), $\tilde{\alpha}_{\text{sat}} \to \alpha_0$ as the dispersion contains only CNCs and water.

S12 Comparison of literature data for additive-induced red-shifts in photonic CNC films

As shown above, if the additive only changes the compression of the structure after KA without changing the point of KA (Φ'_{CNC}, P'), the wavelength of peak reflection is expected to scale with the mass fraction of additive in the final film according to

$$\lambda_{\mathrm{peak}}(\mu_{\mathrm{add}}) = \lambda_0 \left(1 + \frac{\mu_{\mathrm{add}}}{r_{\mathrm{add}}}\right), \quad (29)$$

where λ_0 is the wavelength of peak reflection without additives, μ_{add} is the additive:CNC mass ratio and r_{add} is the additive:CNC density ratio

$$r_{\mathrm{add}} = \frac{\rho_{\mathrm{add}}}{\rho_{\mathrm{CNC}}}, \quad (30)$$

If a given additive reduces the final compression of the film upon drying without affecting the pitch or onset of KA, a plot of λ_{peak} versus μ_{add} is expected to be linear, with slope $\lambda_0/r_{\mathrm{add}}$ and intercept λ_0. The density ratio should be an intrinsic property of the materials used, and consequently the $\lambda_{\mathrm{peak}}(\mu_{\mathrm{add}})$ given by Eq. 29 has only λ_0 as a free fitting parameter.

Fig. S11 shows $\lambda_{\mathrm{peak}}(\mu_{\mathrm{add}})$ data for several neutral additives used to create composite photonic films in this work and previous studies. The spectroscopic methods vary between studies, and the method of extracting $\lambda_{\mathrm{peak}}(\mu_{\mathrm{add}})$ is therefore summarised for each study in **Table S3**. The density values assumed for each additive, based on supplier data, are summarised in **Table S4**. For each dataset, a least-squares fitting to Eq. 29 as used to obtain λ_0, which allowed the datasets for each additive to be compared in terms of normalised wavelength $\lambda_{\mathrm{peak}}(\mu_{\mathrm{add}})/\lambda_0$. As can be seen in **Fig. S11**, a linear relationship describes the experimental data very well for most additives at low loadings ($\mu_{\mathrm{add}} < 0.8$, or up to approx. 40 wt% of additive in the final film), with the notable exception of PEG samples at high loadings.

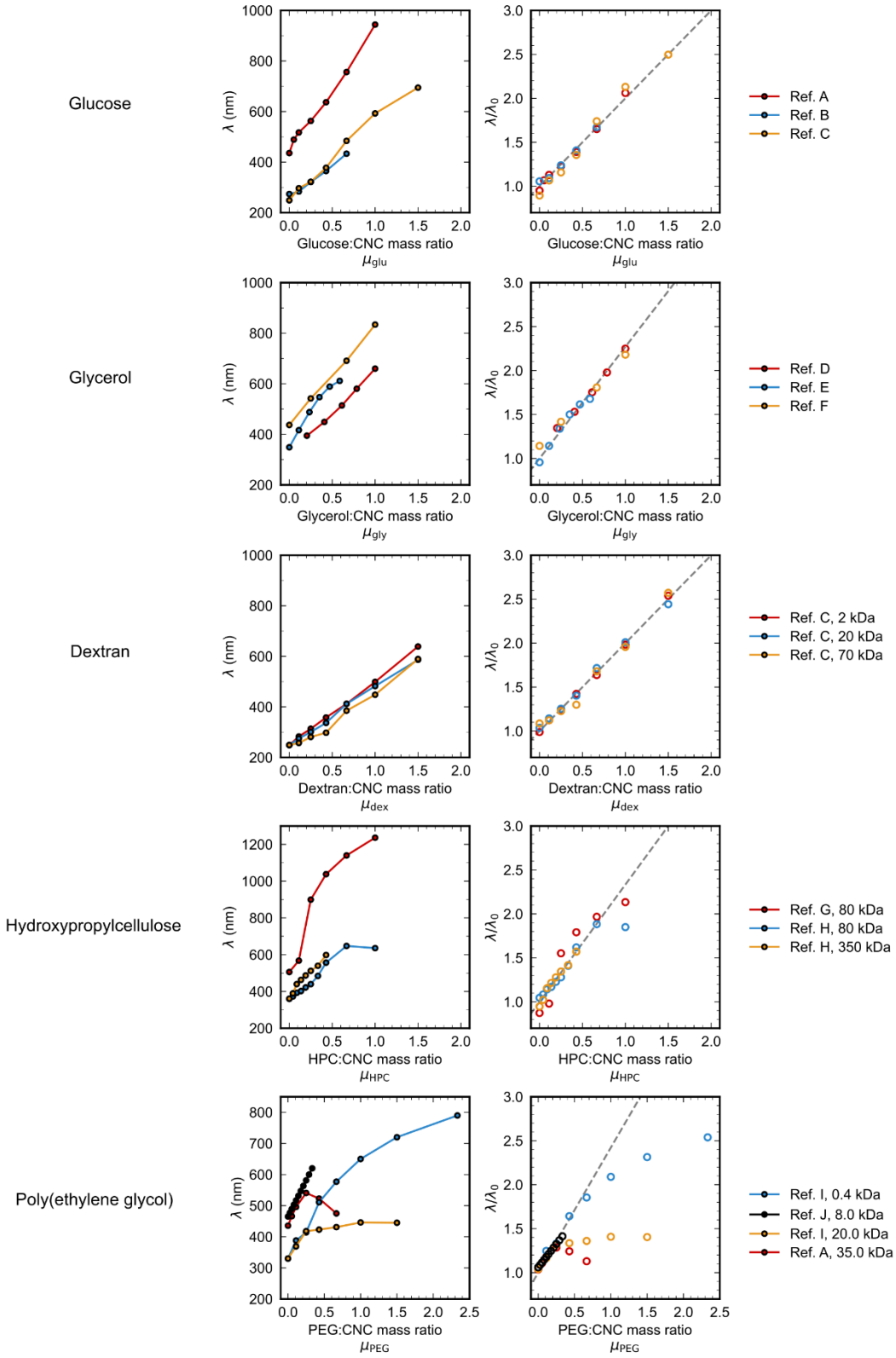

Fig. S11 Variation in peak reflection wavelength with neutral additive concentration in photonic CNC films, comparing the AROS data in this study with previous studies. For each additive, the data are displayed as peak wavelength λ versus additive:CNC mass ratio μ_{add} (left), or normalised wavelength λ/λ_0 versus μ_{add} (right). Grey dotted lines indicate fitting to Eq. 29 using the parameters in **Table S3**. The legend shows reference letters corresponding to **Table S2**, and the molecular weight of the macromolecular additives.

Code	Reference	Method of extracting $\lambda_{peak}(\mu_{add})$
A	This study	Fitting of AROS tilt scan.
B	[3]	Local minimum of transmission spectrum ($\theta_i = 0°, \theta_o = 180°$).
C	[4]	Local minimum of transmission spectrum ($\theta_i = 0°, \theta_o = 180°$).
D	[5]	Maximum of specular reflection spectrum ($\theta_i = 15°, \theta_o = 15°$).
E	[6]	Local maximum of extinction spectrum ($\theta_i = 0°, \theta_o = 180°$).
F	[7]	Maximum of reflection spectrum (experimental setup not specified).
G	[8]	Maximum of reflection spectrum (integrating sphere).
H	[9]	Local minimum of transmission spectrum ($\theta_i = 0°, \theta_o = 180°$).
I	[10]	Maximum of reflection spectrum (experimental setup not specified).
J	[11]	Maximum of micro-scale reflection spectrum.

Table S2 Sources of the data in **Fig. S11** (see section S13 for references) and brief description of the spectroscopic measurement.

Species	Density (g/cm^3)	r_{add}	n
CNC	1.600	-	1.555[12]
Glucose	1.600	1.000	1.555
PEG	1.125	0.706	1.420
Glycerol	1.260	0.788	-
Dextran	1.600	1.000	-
HPC	1.300	0.813	-

Table S3 Density values assumed for each species and associated r_{add} values used for fitting curves in **Fig. S11**.

S13 References

1 T. G. Parton, R. M. Parker, G. T. van de Kerkhof, A. Narkevicius, J. S. Haataja, B. Frka-Petesic and S. Vignolini, *Nat Commun*, 2022, **13**, 2657.
2 T. Wagner and H.-G. Lipinski, *Journal of Open Research Software*, 2013, **1**, e6.
3 Z. Yu, K. Wang and X. Lu, *Int. J. Biol. Macromol.*, 2021, **188**, 385–390.
4 Y. Meng, Z. Long, Z. He, X. Fu and C. Dong, *Biomacromolecules*, 2021, **22**, 4479–4488.
5 X. Dong, D. Li, J.-M. Wu, Z.-L. Zhang, Z.-L. Wang, F. Song, X.-L. Wang and Y.-Z. Wang, *ACS Sustainable Chem. Eng.*, 2022, **10**, 10641–10648.
6 Y.-D. He, Z.-L. Zhang, J. Xue, X.-H. Wang, F. Song, X.-L. Wang, L.-L. Zhu and Y.-Z. Wang, *ACS Appl. Mater. Interfaces*, 2018, **10**, 5805–5811.
7 M. Xu, W. Li, C. Ma, H. Yu, Y. Wu, Y. Wang, Z. Chen, J. Li and S. Liu, *J. Mater. Chem. C*, 2018, **6**, 5391–5400.
8 D. V. Saraiva, R. Chagas, B. M. de Abreu, C. N. Gouveia, P. E. S. Silva, M. H. Godinho and S. N. Fernandes, *Crystals*, 2020, **10**, 122.
9 C. M. Walters, C. E. Boott, T. D. Nguyen, W. Y. Hamad and M. J. Maclachlan, *Biomacromolecules*, 2020, **21**, 1295–1302.
10 Y. Qi, S. Wang, J. Sun, J. Song, H. Li and J. Guo, *International Journal of Biological Macromolecules*, 2024, **260**, 129544.
11 C. A. Williams, R. M. Parker, A. Kyriacou, M. Murace and S. Vignolini, *Adv. Mater.*, 2023, **36**, 2307563.
12 A. G. Dumanli, H. M. van der Kooij, G. Kamita, E. Reisner, J. J. Baumberg, U. Steiner and S. Vignolini, *ACS Appl. Mater. Interfaces*, 2014, **6**, 12302–12306.